

Active polar fluid flow in finite droplets

Carl A. Whitfield¹, Davide Marenduzzo², Raphaël Voituriez^{3,4}, and Rhoda J. Hawkins¹

¹ Department of Physics and Astronomy, University of Sheffield, Hicks Building, Hounsfield Road, Sheffield S3 7RH, United Kingdom

² SUPA, School of Physics and Astronomy, University of Edinburgh, Mayfield Road, Edinburgh EH9 3JZ, United Kingdom

³ Laboratoire de Physique Théorique et Matière Condensée, UMR 7600, Université Pierre et Marie Curie/CNRS, Paris, France

⁴ Laboratoire Jean Perrin, FRE 3231 CNRS /UPMC, 4 Place Jussieu, F-75255 Paris Cedex

the date of receipt and acceptance should be inserted later

Abstract. We present a continuum level analytical model of a droplet of active contractile fluid consisting of filaments and motors. We calculate the steady state flows that result from a splayed polarisation of the filaments. We account for the interaction with an arbitrary external medium by imposing a viscous friction at the fixed droplet boundary. We then show that the droplet has non-zero force dipole and quadrupole moments, the latter of which is essential for self-propelled motion of the droplet at low Reynolds' number. Therefore, this calculation describes a simple mechanism for the motility of a droplet of active contractile fluid embedded in a 3D environment, which is relevant to cell migration in confinement (for example, embedded within a gel or tissue). Our analytical results predict how the system depends on various parameters such as the effective friction coefficient, the phenomenological activity parameter and the splay of the imposed polarisation.

PACS. XX.XX.XX No PACS code given

1 Introduction

The study of active matter, *i.e.* aggregations of particles which are driven out of equilibrium individually by internal energy, has successfully been applied to various biological and physical systems [1], such as flocks of animals or bacteria [2] or vibrated granular rods [3]. The hydrodynamic model of active gels developed by Kruse *et al.* [4, 5, 6] considers the case where the active matter in question is a viscoelastic gel comprising of polar filaments which are pulled by motor molecules generating active stresses in the gel. This can be used as a model of the actin cytoskeleton, where the active stresses generated are contractile (to model the interaction between myosin-II motor proteins and F-actin), as discussed in [7]. In this way, the theoretical model is analogous to in-vitro experiments on reconstituted cytoskeletal networks, which probe the fundamentals of cellular mechanics by isolating specific components of the cytoskeleton and observing the interactions and behaviour [8, 9, 10, 11, 12].

In this paper, we consider a motility mechanism that arises in a droplet of active gel due solely to active contractile stress from the interaction of myosin-II and F-actin. This non-equilibrium activity is fuelled by energy released in the binding of Adenotriphosphate (ATP) to myosin II and its hydrolysis into Adenodiphosphate (ADP) by the motor proteins as they transiently attach and exert forces

on adjacent filaments. Thus, as in [5] and [13], we ignore the self-polymerisation of the actin filaments so that we can isolate the effects of the contractile stresses generated by the actomyosin network only. We apply a viscous friction condition at the boundary to address the issue of cell motility in 3D confinement (such as tissue-like environments), the importance of which is being increasingly recognised [14, 15, 16], particularly due to new experimental techniques that enable its direct observation [17, 18].

We compare our results to the Lattice-Boltzmann fluid simulations of an active droplet by Tjhung *et al.* [19], which shows that a droplet of active gel immersed in a Newtonian fluid will display spontaneous symmetry breaking when the intensity of motor activity is above a certain threshold. This symmetry breaking causes the droplet to reach a motile steady state, similar to that discussed in this paper. The case we present considers a system where the symmetry is already broken by a splayed polarisation of the filaments, which we justify in section 2. Imposing the polarisation field allows us to model this system analytically, providing greater insight into the important factors behind this motile steady state. Also the droplet modelled here interacts with the external medium via a linear viscous friction, whereas the simulations in [19] use a two-phase model with periodic boundary conditions, where the passive viscous properties of the two phases of fluid are identical. Therefore within our framework we can in prin-

ciple consider motion within a generic environment, such as a fluid of different viscosity or a gel, as would be more appropriate to describe a cell's environment.

We first present the calculation in 2 dimensions to simplify both the mathematics and graphical representation of the system. This allows for comparison between the analytical results and new Lattice-Boltzmann simulations of an active droplet that use the source code introduced in [19]. In A we show how the analytical case generalises to 3 dimensions.

2 Model

We begin with a circular droplet of active gel of radius R and assume that the boundary remains fixed, so that we only model the dynamics of the internal fluid. This assumption is valid for a droplet with high cortical tension, such that any active pressure gradients in the droplet would have a negligibly small effect on the boundary shape. This is a valid assumption for *in-vitro* emulsion droplets of cytoskeletal filaments [20] as the droplets in these cases do not visibly deform from spherical even in the presence of high activity. MDA-MB-231 breast tumour cells in matrigel provide an example of an *in-vivo* spherical cytoskeleton droplet, this high cortical tension, as they can migrate through matrigel while maintaining a nearly spherical shape [17].

We define the polarisation \mathbf{p} as the average alignment direction of the ‘barbed’ ends of the actin filaments at a given point in the droplet and assume that, on average, the filaments in the active fluid are highly ordered and so the gel is far from the isotropic phase. This means that the magnitude of the polarisation can be defined as $|\mathbf{p}| = 1$ without loss of generality. In this paper we treat the active contractile stress as nematic, as in [5, 6, 13, 21], which means that \mathbf{p} and $-\mathbf{p}$ are indistinguishable. Therefore, whether we assume polar or nematic order makes no difference to the resulting flow. In this paper we depict the filaments as possessing polar order as actin filaments are polar with distinct ‘barbed’ and ‘pointed’ ends [22].

2.1 Filament polarisation

At high enough filament concentration, a passive actin gel can display nematic order [23], and as such can be described by the distortion free energy:

$$F_d = \int \frac{1}{2} \left\{ K_1 (\nabla \cdot \mathbf{p})^2 + K_2 [\mathbf{p} \cdot (\nabla \times \mathbf{p})]^2 + K_3 [\mathbf{p} \times (\nabla \times \mathbf{p})]^2 \right\} d^3x, \quad (1)$$

where K_1 , K_2 and K_3 are the elastic coefficients for the terms corresponding to splay, twist and bend deformations respectively [24]. In a passive nematic system, the dynamics of the polarisation field \mathbf{p} , in the absence of boundary

effects, are determined by the molecular field $\mathbf{h} = -\frac{\delta F_d}{\delta \mathbf{p}}$. In the one constant approximation $K_1 = K_2 = K_3 = K$, this is given by $\mathbf{h} = K \nabla^2 \mathbf{p}$. We then introduce linear active terms to the dynamics as in [5], which describe the case where the system is linearly out of equilibrium.

In studies of infinite films [25] and quasi one-dimensional active gels above the Friedrick's transition [13], a finite polarisation gradient and spontaneously flowing state is calculated, indicating that such a splayed polarisation field is a natural state in the active contractile phase. This generic splay instability in active contractile systems of filaments and motors is explained qualitatively by [1] as due to long-wavelength splay fluctuations, which perturb the balance of flow by pulling fluid along the axes of the filaments, creating a shear. This shear results in an amplification of the splay fluctuation, causing a feedback loop. Lattice-Boltzmann simulations have also shown that an active contractile droplet is unstable to splay defects and maintains a splayed steady state when the activity is above a critical value [19] as shown in figure 3.

In the case of confinement in a droplet, boundary effects become important and these can promote splay in the filament polarisation depending on the anchoring conditions at the boundary. For example, cells with broken symmetry often display a higher concentration of actin nucleators at the leading edge, which polarises the actin there.

Therefore, we investigate the effects of polarisation splay in an active fluid droplet by imposing a splayed polarisation field. As we are working in the $|\mathbf{p}| = 1$ limit, we can assume without loss of generality that $p_x = \cos(\psi)$ and $p_y = \sin(\psi)$ where ψ is the angle between the filament polarisation and the x -axis. Then, we can arbitrarily choose a direction for the splay to occur, in this case we specify that the polarisation should splay outwards from the x -axis. The simplest example of this is if $\psi \propto y$ and hence we impose the polarisation:

$$\mathbf{p} = \left[\cos\left(\frac{\pi y}{2l}\right), \sin\left(\frac{\pi y}{2l}\right) \right], \quad (2)$$

where l defines the distance in y from the x -axis at which the polarisation will be pointing in the positive or negative y -direction. The relative amount of splay and bend in the polarisation can be calculated by finding the magnitude of the ‘splay’ and ‘bend’ terms in the distortion free energy (from eq. (1)):

$$F_{\text{splay}} = K (\nabla \cdot \mathbf{p})^2 = \frac{\pi^2}{4l^2} K \cos^2\left(\frac{\pi y}{2l}\right), \quad (3)$$

$$F_{\text{bend}} = K [\mathbf{p} \times (\nabla \times \mathbf{p})]^2 = \frac{\pi^2}{4l^2} K \sin^2\left(\frac{\pi y}{2l}\right). \quad (4)$$

where we have made the one constant approximation. Equations (3) and (4) show that splay is the dominant distortion when $l > 2R$ (N.B. the ‘twist’ term, $[\mathbf{p} \cdot (\nabla \times \mathbf{p})]^2$, is always zero in the 2 dimensional case, only contributing in

3 dimensions) and so we take this as a minimum value for l . Therefore, we introduce the ‘splay parameter’ $c_s = R/l$, which, in this limit, acts as a quantitative measure of the splay in the droplet.

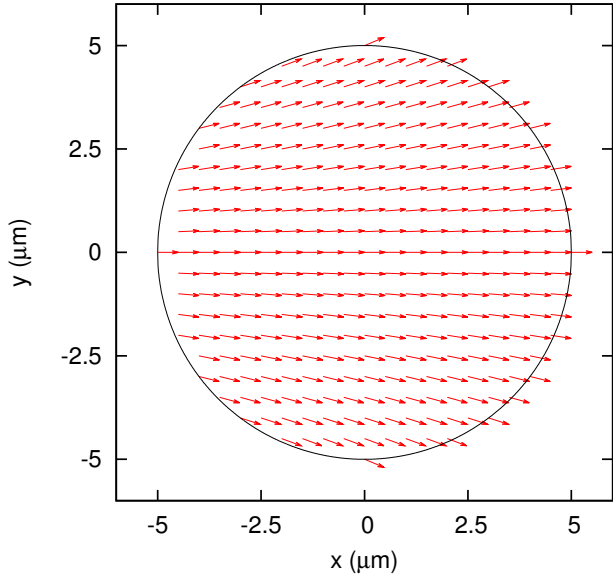


Fig. 1. Vector plot of the polarisation field \mathbf{p} of eq. (2) with length scale $l = 20 \mu\text{m}$ imposed on a circular droplet of radius $R = 5 \mu\text{m}$.

2.2 Equations of motion

To model the dynamics of the internal active gel, we use the coarse grained hydrodynamic approach outlined by Kruse *et al.* [4,5,6]. We take the long-time limit ($t \gg \tau$ where τ is the relaxation time of the gel) which models the active gel as a viscous fluid. Then, the constitutive equation for the stress in the active polar fluid is given by

$$\sigma_{\alpha\beta} = 2\eta u_{\alpha\beta} + \frac{\nu}{2} (p_\alpha h_\beta + p_\beta h_\alpha) - \frac{1}{2} (p_\alpha h_\beta - p_\beta h_\alpha) - \zeta \Delta\mu \left(p_\alpha p_\beta - \frac{\delta_{\alpha\beta}}{d} \right), \quad (5)$$

where σ is the deviatoric stress tensor and the indices denote Cartesian coordinates. The first term on the right hand side of eq. (5) is the viscous stress term, where η is the shear viscosity and $u_{\alpha\beta}$ is the strain rate tensor. The following two terms describe the distortion stress caused by the orientation of the nematic filaments, where ν is a dimensionless constant (negative for rod-like particles - the value and sign of ν however have no qualitative bearings on our results). The final term on the right hand side is the traceless active stress. This depends on ζ , which is a phenomenological parameter for the activity intensity; $\Delta\mu$, the difference in chemical potential between ATP and ADP; and the filament orientation \mathbf{p} . The constant d is the dimensionality of the system. We assume that ζ is constant

for this calculation, which can be interpreted as assuming that there is a uniform density of ATP and myosin II throughout the active gel. Actomyosin networks create contractile stresses [26], and this corresponds to $\zeta < 0$ [5].

As we have taken the fluid limit, we also assume incompressibility, which can be written as,

$$\nabla \cdot \mathbf{v} = 0. \quad (6)$$

Then, the final equation we use is the steady state Cauchy momentum equation,

$$\partial_\alpha (\sigma_{\alpha\beta} - P\delta_{\alpha\beta}) = 0, \quad (7)$$

also known as the force-balance equation, which is used to calculate the resulting steady state flows of the system and the internal pressure P . Equation (7) has no inertial terms since we work in the low Reynolds number limit, due to the small length scale and velocities that are involved at the cellular level.

Substituting eq. (2) into eq. (5), we find expressions for the total deviatoric stress tensor σ . Using eqs. (6) and (7) we arrive at the general steady state equations of motion for the system:

$$\eta \nabla^2 v_x(x, y) = \frac{\tilde{\zeta} \Delta\mu \pi}{2l} \cos\left(\frac{\pi y}{l}\right) + \partial_x P(x, y), \quad (8)$$

$$\eta \nabla^2 v_y(x, y) = \frac{\tilde{\zeta} \Delta\mu \pi}{2l} \sin\left(\frac{\pi y}{l}\right) + \partial_y P(x, y), \quad (9)$$

$$0 = \partial_x v_x(x, y) + \partial_y v_y(x, y), \quad (10)$$

where $\tilde{\zeta} \Delta\mu = \zeta \Delta\mu + \nu K \pi^2 / (4l^2)$. As we are in the regime of broken symmetry, we assume that the nematic contribution to the stress is small compared to the active contribution ($|\nu K \pi^2 / (4l^2)| < |\zeta \Delta\mu|$) and hence $\tilde{\zeta} < 0$ regardless of the value of ν . We then Taylor expand the active terms in eqs. (8) and (9) and reduce our scope to the relevant splay-dominated regime by only taking terms up to quadratic order in y/l :

$$\eta \nabla^2 v_x(x, y) = \frac{\tilde{\zeta} \Delta\mu \pi}{2l} \left[1 - \frac{\pi^2 y^2}{2l^2} + \mathcal{O}\left(\frac{y^3}{l^3}\right) \right] + \partial_x P(x, y), \quad (11)$$

$$\eta \nabla^2 v_y(x, y) = \frac{\tilde{\zeta} \Delta\mu \pi}{2l} \left[\frac{\pi y}{2l} + \mathcal{O}\left(\frac{y^3}{l^3}\right) \right] + \partial_y P(x, y). \quad (12)$$

2.3 Boundary conditions

We confine the solutions to a fixed circular droplet with the following conditions:

$$v_r(R, \theta) = 0, \quad (13)$$

$$\sigma_{r\theta}(R, \theta) = -\xi v_\theta(R, \theta), \quad (14)$$

where r and θ are standard polar co-ordinates and R is the droplet radius. Equation (13) ensures that there is no fluid entering or leaving the droplet and eq. (14) applies an effective viscous friction at the boundary (with friction coefficient ξ). This friction condition is general as it infers little about the external medium, only that it will create some linear resistance to flow at the interface. If the droplet is embedded in a solid, then ξ will determine the slip between the fluid and the boundary. Alternatively, if the external medium is a viscous fluid, and we assume non-slip between the internal and external fluid, then the friction coefficient ξ will be related to the viscosity of the external fluid. Therefore we call ξ the *effective* friction coefficient. It is important to note that in a cell the conditions at the boundary would be more complicated, depending also on the adhesion between the membrane and the surrounding environment, the elastic properties of the external medium and the active processes of the membrane itself. However, we show here that persistent migration can be achieved by actomyosin contraction without any specific adhesions.

The boundary conditions eqs. (13) and (14) are distinctly different from those used in Lattice-Boltzmann simulations of an active contractile droplet (as used to obtain figure 3; and introduced in [19]). In these simulations, a phase field parameter is used to discern between the active and passive phases of the fluid, and this parameter is advected with the fluid velocity. Therefore the shape of the droplet is coupled to the flow, however the boundary between the two phases is diffuse and is defined by the gradient of the phase field. This also means that the external fluid in the simulations is assumed to have the same passive properties as the droplet.

3 Results and Analysis

In general, we can solve eqs. (10), (11), and (12) by assuming power series solutions for v_x , v_y and P :

$$v_x(x, y) = \sum_{n=0}^{\infty} \sum_{m=0}^{\infty} a_{m,n} x^m y^n, \quad (15)$$

$$v_y(x, y) = \sum_{n=0}^{\infty} \sum_{m=0}^{\infty} b_{m,n} x^m y^n, \quad (16)$$

$$P(x, y) = \sum_{n=0}^{\infty} \sum_{m=0}^{\infty} c_{m,n} x^m y^n. \quad (17)$$

The coefficients $a_{m,n}$, $b_{m,n}$ and $c_{m,n}$ are arbitrary constants to be determined by the governing equations and boundary conditions. However, first we can impose that the solutions will be symmetric about the x axis because the governing equations and boundary conditions have this symmetry. This leads to $a_{m,2n+1} = b_{m,2n} = c_{m,2n+1} = 0$ for all integer values of m and n .

To find the final solution for a finite circular droplet, we can substitute the solutions eqs. (15), (16), and (17)

into the approximated equations of motion; eqs. (10), (11), and (12) and boundary conditions; eqs. (13) and (14). This gives an infinite number of simultaneous equations, but (due to the approximation made) one finds that $a_{m,n} = 0$, $b_{m,n} = 0$ and $c_{m,n} = 0$, if $m + n > 6$, and so the series becomes finite. For more details see B.

3.1 Complete Solutions

The full 2-dimensional solutions are given in B by eqs. (B.25), (B.26) and (B.27) and in this section they are presented graphically in figures 2 and 4.

Figure 2 shows profiles of the velocity \mathbf{v} for different values of the effective friction coefficient ξ and the splay parameter c_s . The velocity profile generally has 2 pairs of opposing vortices for lower values of ξ and c_s , and as ξ or c_s is increased (the upper limit of c_s is bound by the second order approximation in r/l) the front pair of vortices occupy more of the droplet. In the limit of no splay, $c_s \rightarrow 0$ for fixed R (or equivalently $l \rightarrow \infty$), the vortices become completely symmetric and the solutions are (figure 2(a)):

$$v_x = -\frac{\tilde{\zeta} \Delta \mu x}{R^2(\xi R + 4\eta)} (R^2 - x^2 - 3y^2), \quad (18)$$

$$v_y = \frac{\tilde{\zeta} \Delta \mu y}{R^2(\xi R + 4\eta)} (R^2 - 3x^2 - y^2), \quad (19)$$

$$P = c_{0,0} + \frac{3\tilde{\zeta} \Delta \mu \eta}{R^2(\xi R + 4\eta)} (x^2 - y^2). \quad (20)$$

The source of the flow in this case is the remaining active terms in the boundary condition eq. (14), since in this limit there are no active terms present in the force balance eqs. (8) and (9). This shows that, even with a constant polarisation, the finite nature of the calculation results in flow inside the droplet (see figure 2(a)), which is not seen in bulk active fluids. These symmetric vortices are observed in Lattice-Boltzmann simulations of a droplet prior to symmetry breaking, which maintains an (approximately) aligned polarisation field (figures 3(a) and (b)). Therefore the splay directly imposes the preferred direction in the flow, and hence the asymmetry of the vortices increases with c_s . The rear vortices only completely disappear mathematically in the infinite friction limit $\xi \rightarrow \infty$, because this destroys the boundary effects that induce the symmetric part of the flow.

The hydrodynamic pressure P in eq. (20) still contains the undetermined constant $c_{0,0}$. This is the average pressure inside the droplet, and can be calculated by considering the forces that act in the direction normal to the droplet boundary. We assume that the net radial force will be zero, as we are considering the steady state solutions, which gives the condition:

$$\hat{\mathbf{r}} \cdot \oint \left[\boldsymbol{\sigma} - \left(P - P_{ext} - \frac{2\gamma}{R} \right) \hat{\mathbf{I}} \right] \cdot \mathbf{d}\mathbf{s}(\theta) \Big|_{r=R} = 0, \quad (21)$$

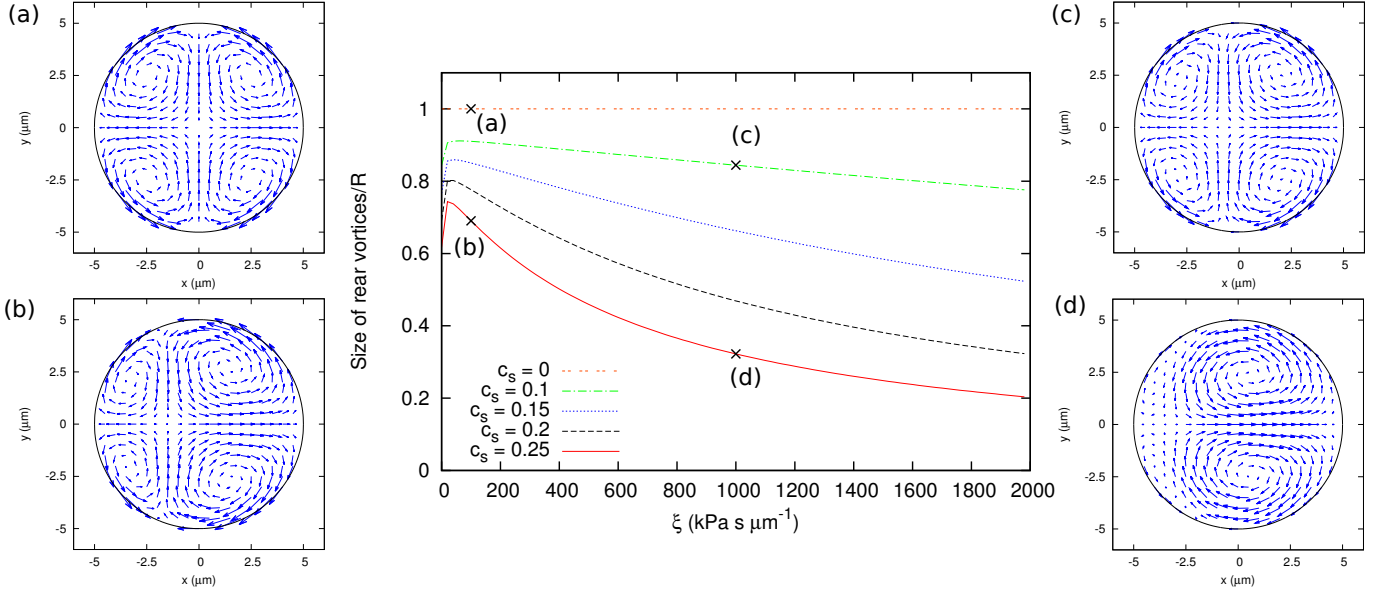


Fig. 2. Graph of the size of the two rear vortices in the droplet against the effective friction coefficient ξ , plotted for various values of the splay parameter c_s . Other parameter values are $\zeta\Delta\mu = -1$ kPa [27], $R = 5$ μm , and $\eta = 10$ kPa s [28]. Corresponding flow profiles at the points labelled (a), (b), (c), and (d) are also shown. For these, the velocity arrow lengths are scaled independently for visibility by a scale factor S such that a velocity magnitude of v corresponds to an arrow length of Sv . The values of S for each plot are: (a) and (b) $S = 300$, (c) $S = 3000$, and (d) $S = 1200$.

where $\mathbf{s}(\theta) = R\hat{\theta}$ is the vector representation of the boundary curve at $r = R$, γ is the surface tension of the droplet, and P_{ext} is the pressure in the external medium (assumed to be constant). Solving eq. (21) for $c_{0,0}$ gives

$$c_{0,0} = \frac{2\gamma}{R} + P_{ext} + \frac{\zeta\Delta\mu\pi^2 R^2}{16l^2}. \quad (22)$$

Figure 4 plots the pressure difference inside the droplet for the same parameters as used in figure 2(b). It shows that the variation in pressure across the boundary is approximately 1 kPa with these estimated values. This means that, for our fixed boundary approximation to be valid, $2\gamma/R \gg 1$ kPa meaning that (for these estimated values) $\gamma \gg 2.5$ kPa μm . For comparison, experimental evidence suggests that the effective cell membrane tension (the combination of the bare membrane tension and the cortex tension) is $\gamma \approx 0.3$ kPa μm [29,30]. Thus, the high surface tension limit assumed in this calculation is not valid for the majority of cells. However, experiments on spontaneously moving active droplets consisting of microtubule filaments and motors show that droplets maintain near perfect spherical symmetry [20]. In that case the active matter is confined to water droplets in oil so the interfacial tension is much larger.

3.2 Analysis of Solutions

The solutions simplify greatly in the infinite friction limit $\xi \rightarrow \infty$, which is equivalent to applying the non-slip boundary condition, $v_\theta = 0$ at $r = R$. Therefore, in this section

we use these solutions to clarify the analysis and to keep the resulting equations brief. This analysis does generalise to the finite friction case, and we show how the results depend on the friction graphically. In the limit $\xi \rightarrow \infty$, the solutions become:

$$v_x = \frac{\zeta\Delta\mu\pi^3}{384\eta l^3} (R^2 - x^2 - y^2) (x^2 + 5y^2 - R^2), \quad (23)$$

$$v_y = -\frac{\zeta\Delta\mu\pi^3}{96\eta l^3} xy (R^2 - x^2 - y^2), \quad (24)$$

$$P = c_{0,0} - \frac{\zeta\Delta\mu\pi}{2l} \left[x + \frac{\pi}{2l} (y^2) + \frac{\pi^2}{24l^2} x (x^2 - 2R^2 - 3y^2) \right]. \quad (25)$$

As we are looking at the steady state solutions of the droplet, it can be shown that there are no net translational forces generated by the droplet,

$$\begin{aligned} \mathbf{F}_i^{(1)} &= \oint \left[\boldsymbol{\sigma} - \left(P - P_{ext} - \frac{2\gamma}{R} \right) \hat{\mathbf{I}} \right] \cdot d\mathbf{s}(\theta) \Big|_{r=R} \\ &= 0. \end{aligned} \quad (26)$$

eq. (21) ensures that there are no net radial forces from the droplet, and it can be shown similarly that there is no net torque. Therefore, we find that there are no net forces produced by the droplet, as expected at low Reynolds' number. However, it can be shown that there is spatial separation of the equal and opposite forces at the droplet boundary. We show this by taking successive moments of the force at the boundary. As for the force monopole (eq. (26)), increasing moments of the force can be expressed by

tensors of increasing order, the dipole and quadrupole moments form the following second and third order tensors respectively:

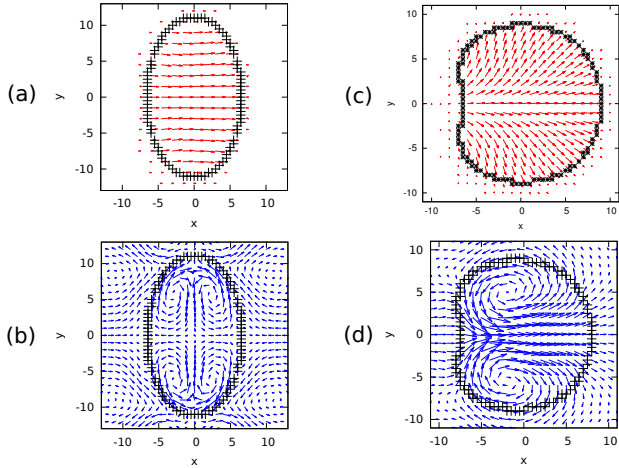


Fig. 3. Lattice Boltzmann simulations of an active contractile droplet. **(a)** Polarisation field before symmetry breaking. **(b)** Velocity profile before symmetry breaking. **(c)** Splayed polarisation field in motile steady state **(d)** Velocity profile of the motile steady state in the droplet reference frame.

$$F_{ij}^{(2)} = \int_0^{2\pi} f_i x_j d\theta, \quad (27)$$

$$F_{ijk}^{(3)} = \int_0^{2\pi} f_i x_j x_k d\theta \quad (28)$$

where $f_i = -[\sigma_{il} - (P - P_{ext} - 2\gamma/R)\delta_{il}]x_l$ evaluated at $r = R$ and the coordinates x_i are cartesian ($x_1 = x$ and $x_2 = y$). The dipole moment eq. (27) gives:

$$F_{ij}^{(2)} = \alpha(\delta_{1,1} - \delta_{2,2}) \quad (29)$$

$$\text{where } \alpha = \frac{\tilde{\zeta}\Delta\mu\pi R^2}{2} \left(1 - \frac{\pi^2 c_s^2}{8}\right).$$

The coefficient α is always negative and hence the droplet is contractile along the x -axis and equally extensile along the y -axis. This force dipole is due to the alignment and contraction of the filaments along the x -axis, and this can be shown by taking the limit of no splay, $c_s \rightarrow 0$, where all of the filaments in the droplet are completely aligned. In this limit the dipole moment is maximised, and this explains the behaviour observed in the Lattice-Boltzmann simulations of an active droplet that is below the threshold concentration of activity to break symmetry. In those simulations, the filaments remain approximately aligned in one direction and the droplet squeezes itself, shortening in the direction of alignment and extending in the perpendicular direction (figure 3(a)) [19].

For a circular droplet at low Reynolds' number, a non-zero force dipole distribution is insufficient for motion [31] and in this case it does not vanish in the symmetric limit $c_s \rightarrow 0$. However, the quadrupole moment is directly dependent on the symmetry breaking,

$$F_{ijk}^{(3)} = \beta(-\delta_{1,1,1} + \delta_{1,2,2}) \quad (30)$$

$$\text{where } \beta = \frac{\tilde{\zeta}\Delta\mu\pi^2 R^3 c_s}{4} \left(1 - \frac{\pi^2 c_s^2}{12}\right).$$

Unlike the dipole moment, the forces that make up the quadrupole moment only act in the x -direction (shown by the non-zero components of the quadrupole tensor both having $i = 1$). It shows that the net normal forces at the front and back of the droplet act in the positive x direction (as $\beta < 0$) and the shear forces at the sides are equal and opposite, as sketched in figure 5(a). In the no splay limit, $c_s \rightarrow 0$, the quadrupole moment disappears along with the asymmetry in x .

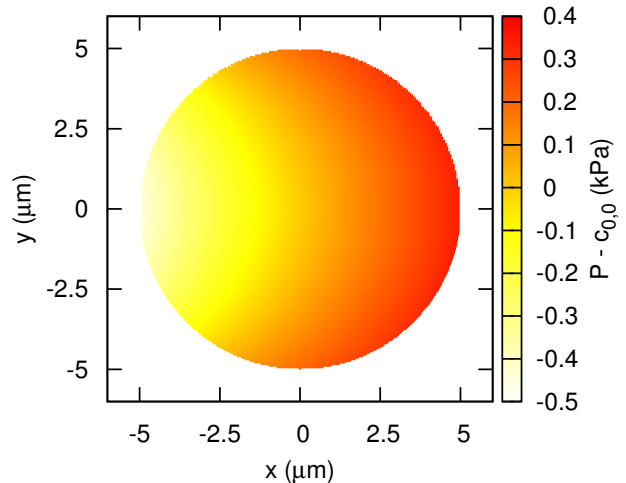


Fig. 4. Relative pressure inside the droplet for $\xi = 100 \text{ kPa s } \mu\text{m}^{-1}$. Other parameter values are $\tilde{\zeta}\Delta\mu = -1 \text{ kPa}$, $R = 5 \mu\text{m}$, $\eta = 10 \text{ kPa s}$, and $c_s = 0.25$.

The quadrupole moment characterises the motility mechanism because of the force distribution it indicates. The shear forces at the sides of the droplet arise from the friction between the fluid and the external medium and hence act to propel the droplet forwards (or the medium rearwards in the droplet rest frame). The normal forces however act to deform the front and back of the droplet asymmetrically in the positive x -direction. The magnitude of these shear and normal forces can be calculated by integrating the corresponding elements of the total stress

tensor at the boundary,

$$F_i^{(\text{shear})} = - \int_0^{2\pi} \sigma_{ij} x_j d\theta \Big|_{r=R} \quad \text{where } i \neq j, \quad (31)$$

$$F_i^{(\text{norm})} = - \int_0^{2\pi} [\sigma_{ii} - (P - P_{ext} - 2\gamma/R)] x_i d\theta \Big|_{r=R}. \quad (32)$$

These forces only act in the x direction and, in the infinite friction limit, they are given by

$$F_x^{(\text{shear})} = -F_x^{(\text{norm})} = \frac{\tilde{\zeta} \Delta \mu \pi^2 R c_s}{2} \left(1 - \frac{5}{48} \pi^2 c_s^2 \right). \quad (33)$$

The friction dependence of these forces is plotted in figure 5(b), and shows that the magnitude of the forces plateaus at large friction, with the maximum at the infinite friction limit given by eq. (33).

Therefore, this simple model of an active droplet demonstrates a type of swimming behaviour where the mechanism is analogous to a continuous version of the discrete swimming style of cells such as algae that use beating cilia to move [32]. The friction interaction between the active fluid and the external medium at the boundary pushes the droplet forwards, in the same way as the ‘power stroke’ of a cilium does. The ‘recovery stroke’ is then the equivalent of the flow through the centre of the droplet, which avoids interaction with the external medium and recycles the fluid.

We can estimate the migration speed of the droplet through a viscous medium by calculating the average velocity at the boundary. Since we work in the droplet reference frame, if we assume that the velocity of the external fluid will be the same as the internal fluid at $r = R$, then the steady swimming speed is just given by the negative of the average cortical velocity (as shown in [33]):

$$\begin{aligned} \mathbf{v}_{mig} &= - \frac{1}{2\pi} \int_0^{2\pi} \mathbf{v}(R, \theta) d\theta \\ &= - \frac{\tilde{\zeta} \Delta \mu \pi R c_s}{8(\xi R + 2\eta)} \left(1 - \frac{\pi^2 c_s^2}{12} \right) \hat{\mathbf{x}}. \end{aligned} \quad (34)$$

In this case the effective friction coefficient ξ relates directly to the viscosity of the external fluid, and is inversely proportional to the migration speed. Relating this to the graph in figure 5(b) we see that for a very viscous medium, the droplet still exerts almost the maximum amount of force onto the external fluid but the droplet is barely able to move. Conversely, in a low viscosity medium the droplet velocity is high but relatively little force is exerted on the external fluid.

To summarise, the dipole moment shows that the droplet behaves like a *puller* (contractile along axis of motion), however this is not sufficient for motility in this case. It is the quadrupole moment that characterises the motility mechanism and symmetry breaking in our system, and

the resulting picture resembles the motility mechanism of a *squirmers* (a particle propelled by coordinated beating of cilia on its surface) [34].

4 Conclusions and Further Remarks

The model we have presented here demonstrates analytically how self-propelled motion can be generated in a finite active polar droplet, purely by the internal circulation of material driven by active contractile stresses. By imposing an asymmetric splayed polarisation on the droplet, we have analytically calculated the hydrodynamic steady state of the system. The resulting internal fluid flow coupled with a viscous interaction at the boundary causes a non zero force quadrupole and leads to self-propulsion of the droplet.

In addition, our model predicts flow in the droplet even when the filaments are completely aligned and the droplet is not motile, which is also seen in simulations. In this limit the filament alignment results in a symmetric force dipole moment, which is responsible for the ‘squashing’ of the droplet that is seen in simulations, prior to the development of splay instabilities [19].

Our model shows that according to the friction at the boundary and the amount of elastic splay, the intradroplet flow can undergo transitions between several different patterns. For infinite friction, we observe a transition from zero flow in the no-splay limit to 2 directed vortices for finite splay. In the finite friction case, we observe a transition from 4 symmetric vortices in the no-splay limit to 4 asymmetric vortices for finite splay. This means that for finite splay there is a transition from 4 asymmetric vortices to 2 vortices as the friction goes to infinity. The 4 symmetric vortices are due to the interaction between the active gel and the boundary and consequently the flow is zero in the infinite friction limit due to the boundary condition $v_\theta(R) = 0$. The 2 directed vortices are generated by the active stress that due to the splay. The 4 asymmetric vortices are a combination of these two effects.

Our results predict and explain both the non-motile and motile states observed in Lattice-Boltzmann simulations of active droplets [19]. Importantly, as we consider a confined active gel and control the flow field at the boundary, our calculations can extend those of [19] to the case of a generic external medium that can be applied to more biologically relevant cases, such as an active droplet embedded in a more viscous environment or viscoelastic gel.

Previous theoretical studies using a coarse-grained hydrodynamic approach on active gels in bulk have predicted individual vortices due to radially symmetric filament polarisations [5]. Single vortices have also been observed in discrete microscopic models [35, 36] and experimentally for microtubule filaments [37, 38]. An important distinction of our model is that the pairs of directed vortices we predict only form in confinement. Experimentally probing *in vitro*

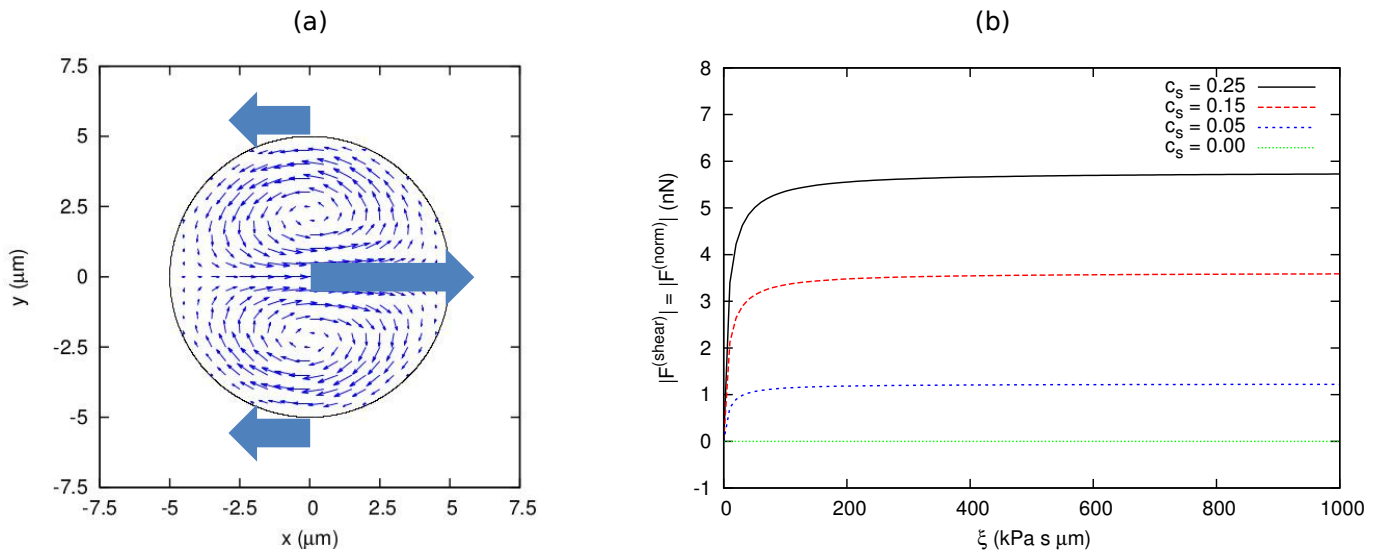


Fig. 5. (a) Sketch of the droplet motility mechanism in 2D. The large arrows represent the spatially separated forces exerted by the active droplet on a surrounding medium, where the central arrow is the sum of the normal forces in the x -direction and the arrows at the top and bottom each contribute half of the total shear force in the x -direction. The smaller arrows show the flow profile of the motile droplet in the case of a solid non-slip boundary. (b) Magnitude of the shear and normal forces (which are equal and opposite) plotted against the effective friction coefficient ξ for several values of the splay parameter c_s . Note that in the no-splay case these forces are zero, as is the quadrupole moment. Parameter values used are $R = 5 \mu\text{m}$, $\eta = 10 \text{kPa s}$ and $\zeta \Delta\mu = -1 \text{kPa}$.

active gels in confinement is now becoming feasible due to new techniques. Recent examples include confinement of active microtubule-kinesin networks inside microchambers (cite) to measure the forces exerted in these systems and inside fluid droplets in emulsions of water and oil using microfluidic devices [20].

The results presented here are complimentary to the case of a spherical cell migrating due to the flow of an active gel cortical layer [39]. In that case, a similar force distribution is generated to propel the droplet forwards, only the asymmetry is driven by activity concentration rather than filament polarisation. In this paper we have not explicitly enforced a cortical layer of active gel, but rather we have modelled a complete droplet of active gel, with similar findings. Therefore, it is likely that coupling aspects from both of these simplified systems will lead to greater understanding of friction-dependent cell migration in confinement.

This analytical study explains how motility can occur in a *in-vitro* active droplet of contractile actomyosin when confined in a 3D environment. Experimental studies of this nature in the future will be important in understanding actomyosin dynamics in cells and also how real active gels differ from the linear model used in these calculations. The motion that we predict is heavily friction-dependent, but does not rely on the droplet being adhered to the surrounding medium. In this way the work is also relevant to the study of migration mechanisms in environments where cells are unable to form adhesion complexes that connect the cytoskeleton to the external medium.

References

1. S. Ramaswamy, Annual Review of Condensed Matter Physics **1**, 323 (2010)
2. J. Toner, Y. Tu, Physical Review E **58**(4), 4828 (1998)
3. V. Narayan, S. Ramaswamy, N. Menon, Science **317**(5834), 105 (2007), ISSN 0036-8075
4. K. Kruse, F. Jülicher, Phys. Rev. Lett. **85**(8), 1778 (2000)
5. K. Kruse, J.F. Joanny, F. Jülicher, J. Prost, K. Sekimoto, Phys. Rev. Lett. **92**(7), 078101 (2004)
6. K. Kruse, J.F. Joanny, F. Jülicher, J. Prost, K. Sekimoto, The European Physical Journal E **16**(1), 5 (2005)
7. J.F. Joanny, J. Prost, HFSP Journal **3**(2), 94 (2009)
8. D. Mizuno, C. Tardin, C. Schmidt, F. MacKintosh, Science **315**(5810), 370 (2007), ISSN 0036-8075
9. F.C. Mackintosh, C.F. Schmidt, Curr. Opin. Cell Biol. **22**(1), 29 (2010)
10. M.S. e Silva, M. Depken, B. Stuhmann, M. Korsten, F.C. MacKintosh, G.H. Koenderink, Proceedings of the National Academy of Sciences **108**(23), 9408 (2011), ISSN 0027-8424
11. S. Köhler, V. Schaller, A.R. Bausch, PloS one **6**(8), e23798 (2011), ISSN 1932-6203
12. S. Köhler, A.R. Bausch, PloS one **7**(7), e39869 (2012), ISSN 1932-6203
13. R. Voituriez, J.F. Joanny, J. Prost, Europhys. Lett. **70**(3), 404 (2005)
14. G. Charras, E. Paluch, Nat. Rev. Mol. Cell Biol. **9**(9), 730 (2008), ISSN 1471-0072
15. R.J. Hawkins, M. Piel, G. Faure-Andre, A.M. Lennon-Dumenil, J.F. Joanny, J. Prost, R. Voituriez, Phys. Rev. Lett. **102**(5), 058103 (2009)
16. K. Konstantopoulos, P.H. Wu, D. Wirtz, Biophys. J. **104**(2), 279 (2013), <http://dx.doi.org/10.1016/j.bpj.2012.12.016>

17. R. Poincloux, O. Collin, F. Lizárraga, M. Romao, M. Debray, M. Piel, P. Chavrier, Proceedings of the National Academy of Sciences **108**(5), 1943 (2011)
18. M. Weber, R. Hauschild, J. Schwarz, C. Moussion, I. de Vries, D.F. Legler, S.A. Luther, T. Bollenbach, M. Sixt, Science **339**(6117), 328 (2013), ISSN 0036-8075
19. E. Tjhung, D. Marenduzzo, M.E. Cates, Proceedings of the National Academy of Sciences **109**(31), 12381 (2012)
20. T. Sanchez, D.T.N. Chen, S.J. DeCamp, M. Heymann, Z. Dogic, Nature **491**, 431 (2012)
21. S. Fürthauer, M. Neef, S. Grill, K. Kruse, F. Jülicher, New Journal of Physics **14**(2), 023001 (2012), ISSN 1367-2630
22. B. Alberts, A. Johnson, J. Lewis, M. Raff, K. Roberts, P. Walter, *Molecular Biology of the Cell*, 5th edn. (Garland Science, New York, 2008)
23. F. Huber, D. Strehle, J. Ks, Soft Matter **8**(4), 931 (2012)
24. P.G. de Gennes, J. Prost, *The Physics of Liquid Crystals*, 2nd edn. (Clarendon Press, Oxford, 1993)
25. R. Voituriez, J.F. Joanny, J. Prost, Phys. Rev. Lett. **96**(2), 028102 (2006)
26. P.M. Bendix, G.H. Koenderink, D. Cuvelier, Z. Dogic, B.N. Koeleman, W.M. Brieher, C.M. Field, L. Mahadevan, D.A. Weitz, Biophys. J. **94**(8), 3126 (2008), ISSN 0006-3495
27. K. Kruse, J.F. Joanny, F. Jülicher, J. Prost, Phys. Biol. **3**(2), 130 (2006)
28. F. Wottawah, S. Schinkinger, B. Lincoln, R. Ananthakrishnan, M. Romeyke, J. Guck, J. Ks, Phys. Rev. Lett. **94**(9), 098103 (2005), ISSN 1079-7114
29. O. Thoumine, O. Cardoso, J.J. Meister, Euro. Biophys. J. **28**(3), 222 (1999), ISSN 0175-7571, <http://dx.doi.org/10.1007/s002490050203>
30. J. Dai, M.P. Sheetz, Biophys. J. **77**(6), 3363 (1999), ISSN 0006-3495
31. N. Yoshinaga, arXiv preprint arXiv:1307.3120 pp. – (2013)
32. D. Bray, *Cell Movements: From Molecules to Motility*, 2nd edn. (Garland, New York, 2001)
33. H.A. Stone, A.D. Samuel, Phys. Rev. Lett. **77**(19), 4102 (1996)
34. J. Blake, J. Fluid Mech **46**, 199 (1971)
35. D.A. Head, G. Gompper, W.J. Briels, Soft Matter **7**(7), 3116 (2011), ISSN 1744-683X, <http://dx.doi.org/10.1039/COSM00888E>
36. F. Nédélec, The Journal of cell biology **158**(6), 1005 (2002), ISSN 0021-9525
37. F.J. Nédélec, T. Surrey, A.C. Maggs, S. Leibler, Nature **389**(6648), 305 (1997), ISSN 0028-0836, <http://dx.doi.org/10.1038/38532>
38. T. Surrey, F. Nédélec, S. Leibler, E. Karsenti, Science **292**(5519), 1167 (2001)
39. R.J. Hawkins, R. Poincloux, O. Bénichou, M. Piel, P. Chavrier, R. Voituriez, Biophys. J. **101**(5), 1041 (2011)

Appendices

A Extension to Three Dimensions - Spherical Droplet

By applying appropriate symmetry rules, the calculation can be easily extended to three dimensions for the case of a spherical droplet with radius R and centre at $x = 0$. If we assume that the polarisation is still splayed around the

x -axis uniformly and satisfies $|\mathbf{p}| = 1$ then we can define it in cartesian coordinates as

$$\mathbf{p} = \left[\frac{1}{\sqrt{2}} \sqrt{1 + \cos\left(\frac{\pi y}{l}\right) \cos\left(\frac{\pi z}{l}\right)}, \sin\left(\frac{\pi y}{2l}\right) \cos\left(\frac{\pi z}{2l}\right), \cos\left(\frac{\pi y}{2l}\right) \sin\left(\frac{\pi z}{2l}\right) \right]. \quad (\text{A.1})$$

This means that the governing partial differential equations, to a second order approximation (the 3D analogue of eqs. (11) and (12)), become

$$\eta \nabla^2 v_x = \frac{\tilde{\zeta} \Delta \mu \pi}{l} \left[1 - \frac{3\pi^2}{8l^2} (y^2 + z^2) \right] + \partial_x P, \quad (\text{A.2})$$

$$\eta \nabla^2 v_y = \frac{3\tilde{\zeta} \Delta \mu \pi^2}{4l^2} y + \partial_y P, \quad (\text{A.3})$$

$$\eta \nabla^2 v_z = \frac{3\tilde{\zeta} \Delta \mu \pi^2}{4l^2} z + \partial_z P, \quad (\text{A.4})$$

with the incompressibility condition now defined as

$$\partial_x v_x + \partial_y v_y + \partial_z v_z = 0. \quad (\text{A.5})$$

We can use the boundary conditions of eqs. (13) and (14) as they are, but now r is the spherical radial coordinate and θ is the angle between r and the z axis. We also need an extra boundary condition that defines the friction similarly for the tangential stress in the φ direction, where φ is the angle between projection of r on to the xy -plane and the x -axis. This is simply given by the condition $\sigma_{r\varphi} = -\xi v_\varphi$ at $r = R$. Clearly, the y and z -directions here are indistinguishable and we apply this to the final solution by ensuring that

$$v_y|_{y=z, z=y} = v_z, \quad (\text{A.6})$$

$$v_x|_{y=z, z=y} = v_x, \text{ and} \quad (\text{A.7})$$

$$P|_{y=z, z=y} = P. \quad (\text{A.8})$$

As one would expect, the solution is just a 3-dimensional projection of the 2-dimensional case. In the infinite friction limit ($\xi \rightarrow \infty$) the solutions are

$$v_x = \frac{3\tilde{\zeta} \Delta \mu \pi^3}{560\eta l^3} (R^2 - x^2 - y^2 - z^2) (x^2 + 3y^2 + 3z^2 - R^2), \quad (\text{A.9})$$

$$v_y = -\frac{3\tilde{\zeta} \Delta \mu \pi^3}{280\eta l^3} xy (R^2 - x^2 - y^2 - z^2), \quad (\text{A.10})$$

$$v_z = -\frac{3\tilde{\zeta} \Delta \mu \pi^3}{280\eta l^3} xz (R^2 - x^2 - y^2 - z^2), \quad (\text{A.11})$$

$$P = c_{0,0,0} - \frac{\tilde{\zeta} \Delta \mu \pi}{l} \left[x + \frac{3\pi}{8l} (y^2 + z^2) + \frac{\pi^2}{280l^2} x (14x^2 - 21(y^2 + z^2) - 30R^2) \right]. \quad (\text{A.12})$$

Plots of the solution are presented in figure A. Finally, we can use the solutions in eqs. (A.9), (A.10), (A.11), and

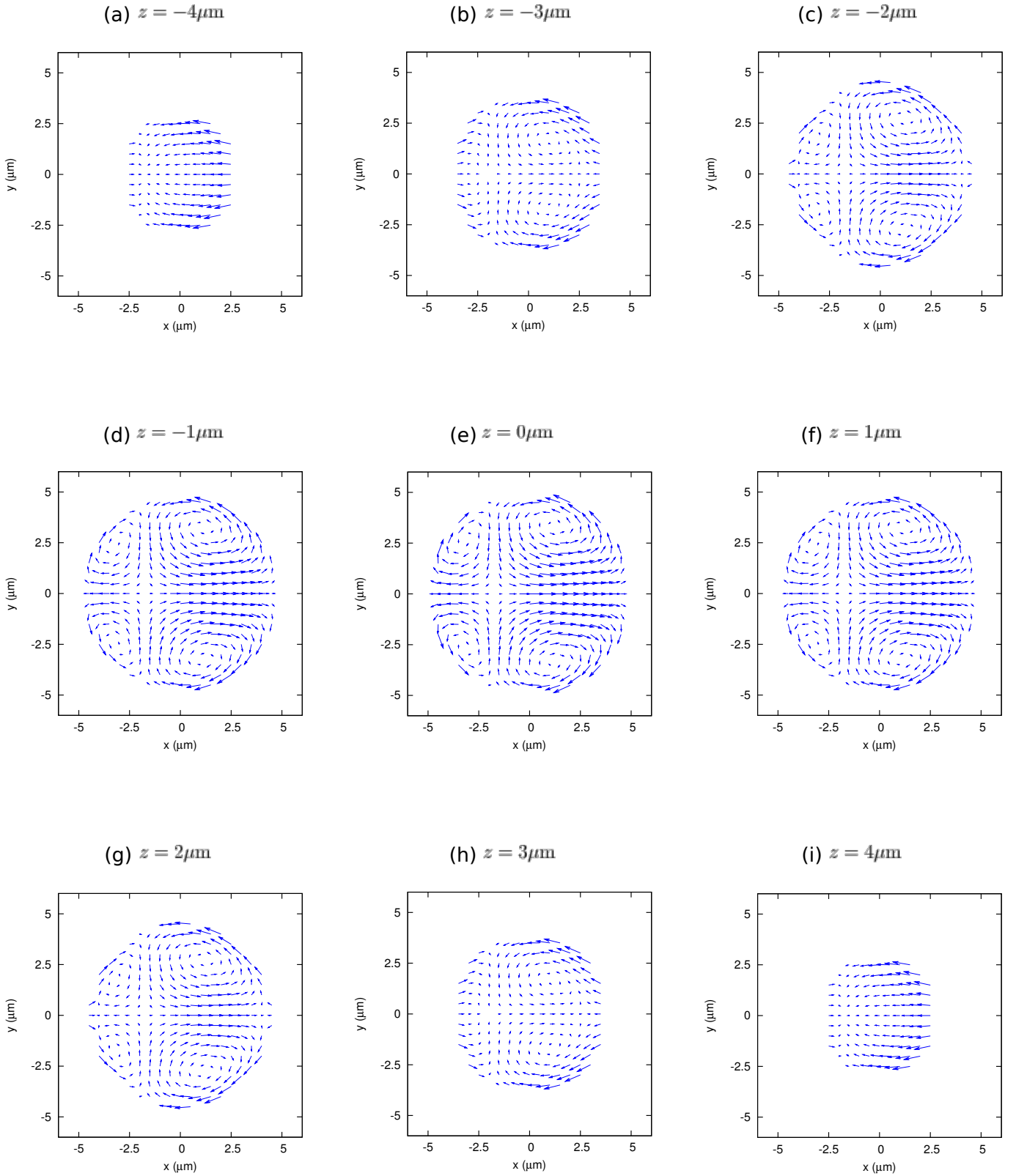


Fig. A.1. Vector plots of the x and y components of the velocity profile in a spherical droplet with centre at the origin. Each plot shows a different slice at the labelled z values. The parameter values used are $\xi = 100 \text{ kPa s } \mu\text{m}^{-1}$, $R = 5 \mu\text{m}$, $c_s = 0.25$, $\zeta \Delta\mu = -1 \text{ kPa}$ and $\eta = 10 \text{ kPa s}$.

(A.12) to show that the dipole and quadrupole moments of the force in the 3D case are very similar to the 2D case:

$$F_{ij}^{(2)} = \tilde{\alpha} (2\delta_{1,1} - \delta_{2,2} - \delta_{3,3}), \quad (\text{A.13})$$

$$\text{where } \tilde{\alpha} = \frac{4\tilde{\zeta}\Delta\mu\pi R^3}{9} \left(1 - \frac{3\pi^2 c_s^2}{20}\right),$$

$$F_{ijk}^{(2)} = \tilde{\beta} (-2\delta_{1,1,1} + \delta_{1,2,2} + \delta_{1,3,3}) \quad (\text{A.14})$$

$$\text{where } \tilde{\beta} = \frac{4\tilde{\zeta}\Delta\mu\pi^2 R^4 c_s}{15} \left(1 - \frac{3\pi^2 c_s^2}{28}\right),$$

As in the 2D circular droplet case, one can see that the dipole moment in eq. (A.13) shows that there is a net contraction along the x -axis, which is balanced by equal extensile moments in the y and z directions. The second moment shows that the splay induces a preferred direction of motion and the formation of a non-zero quadrupole moment. This shows that there is a net normal force generated the front and back of the droplet, and an equal net rearward force around the equatorial plane (yz plane) of the droplet.

B Calculation of Steady State for Circular Droplet

The assumed power series solutions in eqs. (15), (16), and (17) can be reduced by assuming that they will be symmetric about the x -axis, since the system, defined by the polarisation and the boundary conditions, obeys this symmetry. This implies that $a_{m,2n+1} = b_{m,2n} = c_{m,2n+1} = 0$ and leaves,

$$v_x(x, y) = \sum_{n=0}^{\infty} \sum_{m=0}^{\infty} a_{m,2n} x^m y^{2n}, \quad (\text{B.1})$$

$$v_y(x, y) = \sum_{n=0}^{\infty} \sum_{m=0}^{\infty} b_{m,2n+1} x^m y^{2n+1}, \quad (\text{B.2})$$

$$P(x, y) = \sum_{n=0}^{\infty} \sum_{m=0}^{\infty} c_{m,2n} x^m y^{2n}. \quad (\text{B.3})$$

We then substitute these into the governing partial differential equations and boundary conditions; eqs. (10), (11), (12), (13), and (14) and solve these simultaneously to determine the values of all the constants $a_{m,n}$, $b_{m,n}$, and $c_{m,n}$.

The incompressibility condition of eq. (10) becomes,

$$\sum_{n=0}^{\infty} \sum_{m=0}^{\infty} [a_{m+1,2n}(m+1) + b_{m,2n+1}(2n+1)] x^m y^{2n} = 0, \quad (\text{B.4})$$

which, comparing coefficients, gives the following set of equations for all values of n and m ,

$$b_{m,2n+1} = -\frac{m+1}{2n+1} a_{m+1,2n}. \quad (\text{B.5})$$

The x -component of the force balance eq. (11) becomes:

$$\begin{aligned} & \sum_{n=0}^{\infty} \sum_{m=0}^{\infty} x^m y^{2n} [\eta a_{m+2,2n}(m+2)(m+1) \\ & + \eta a_{m,2n+2}(2n+2)(2n+1) - c_{m+1,2n}(m+1)] \\ & = \frac{\tilde{\zeta}\Delta\mu\pi}{2l} \left[1 - \frac{\pi^2 y^2}{2l^2}\right]. \end{aligned} \quad (\text{B.6})$$

This leads to the following set of simultaneous equations, ($m = n = 0$):

$$c_{1,0} = 2\eta(a_{2,0} + a_{0,2}) - \frac{\tilde{\zeta}\Delta\mu\pi}{2l}, \quad (\text{B.7})$$

($m = 0, n = 1$):

$$c_{1,2} = 2\eta(a_{2,2} + 6a_{0,4}) + \frac{\tilde{\zeta}\Delta\mu\pi^3}{4l^3}, \quad (\text{B.8})$$

(all other m and n combinations):

$$\begin{aligned} c_{m+1,2n} &= \frac{\eta}{m+1} [a_{m+2,2n}(m+1)(m+2) \\ & + a_{m,2n+2}(2n+1)(2n+2)]. \end{aligned} \quad (\text{B.9})$$

The y -component of the force balance eq. (12) becomes:

$$\begin{aligned} & \sum_{n=0}^{\infty} \sum_{m=0}^{\infty} x^m y^{2n+1} [\eta b_{m+2,2n+1}(m+2)(m+1) \\ & + \eta b_{m,2n+3}(2n+3)(2n+2) - c_{m,2n+2}(2n+2)] \\ & = \frac{\tilde{\zeta}\Delta\mu\pi^2 y}{2l^2}. \end{aligned} \quad (\text{B.10})$$

For $m = n = 0$, this gives,

$$c_{0,2} = \eta(b_{2,1} + 3b_{3,0}) - \frac{\tilde{\zeta}\Delta\mu\pi^2}{2l^2}, \quad (\text{B.11})$$

and for all other m and n values,

$$\begin{aligned} c_{m,2n+2} &= \frac{\eta}{2n+2} [b_{m+2,2n+1}(m+1)(m+2) \\ & + b_{m,2n+3}(2n+2)(2n+3)]. \end{aligned} \quad (\text{B.12})$$

To apply the circular boundary conditions, we transform the velocity solutions of eqs. (B.1) and (B.2) into plane polar coordinates. We use binomial expansions on terms of the form $\sin^{2n}(\theta)$ so that the expressions can be written in terms of powers of $\cos(\theta)$, as such:

$$\sin^{2n}(\theta) = (1 - \cos^2(\theta))^n = \sum_{k=0}^n (-1)^k \binom{n}{k} \cos^{2k}(\theta). \quad (\text{B.13})$$

Then, through further manipulation we acquire the following equations for the plane polar components of the velocity,

$$v_r = \sum_{j=0}^{\infty} \sum_{k=0}^{\bar{j}} (-1)^k \left\{ \sum_{n=k}^{\infty} \left[\binom{n}{k} a_{j-2k-1,2n} + \binom{n+1}{k} b_{j-2k,2n+1} r^2 \right] r^{j+2n-2k-1} \right\} \cos^j(\theta), \quad (\text{B.14})$$

$$v_\theta = \sin(\theta) \sum_{j=0}^{\infty} \sum_{k=0}^{\bar{j}} (-1)^k \left[\sum_{n=k}^{\infty} \binom{n}{k} (-a_{j-2k,2n} + b_{j-2k-1,2n+1}) r^{j+2n-2k} \right] \cos^j(\theta). \quad (\text{B.15})$$

Here, the substitution $j = m + 2k$ was used so that we can compare coefficients of powers of $\cos(\theta)$, and \bar{j} is just,

$$\bar{j} = \begin{cases} j/2 & \text{if } j = \text{even} \\ (j-1)/2 & \text{if } j = \text{odd}. \end{cases} \quad (\text{B.16})$$

Note also that eqs. (B.14) and (B.15) contain coefficients of the form $a_{-1,2n}$ and $b_{-1,2n+1}$ which are defined as equal to 0, as they are not in the original expansion. They are only included so that v_r and v_θ can be written in such a general form. Substituting eq. (B.14) into the impermeable boundary condition eq. (13) we acquire the following set of simultaneous equations for all values of j :

$$\sum_{k=0}^{\bar{j}} (-1)^k \left\{ \sum_{n=k}^{\infty} R^{j+2n-2k-1} \left[\binom{n}{k} a_{j-2k-1,2n} + \binom{n+1}{k} b_{j-2k,2n+1} R^2 \right] \right\} = 0. \quad (\text{B.17})$$

The final set of simultaneous equations comes from the friction boundary condition of eq. (14), which written in full is:

$$\eta r \left(\frac{\partial(v_\theta/r)}{\partial r} + \frac{1}{r^2} \frac{\partial v_r}{\partial \theta} \right) - \tilde{\zeta} \Delta \mu \left[\left(-\frac{\pi r}{2l} + \frac{\pi^3 r^3}{12l^3} \right) + \left(-1 + \frac{\pi^2 r^2}{2l^2} \right) \cos(\theta) + \left(\frac{\pi r}{l} - \frac{\pi^3 r^3}{4l^3} \right) \cos^2(\theta) - \frac{\pi^2 r^2}{2l^2} \cos^3(\theta) + \frac{\pi^3 r^3}{6l^3} \cos^4(\theta) \right] \sin(\theta) = -\xi v_\theta \Big|_{r=R}. \quad (\text{B.18})$$

Here we have approximated the stress tensor component $\sigma_{r\theta}$ up to third order terms in r/l , because this is differentiated in the force balance equation, which we approximated to second order in this calculation (eqs. (11) and (12)). Substituting eqs. (B.14) and (B.15) into eq. (B.18) and comparing coefficients of $\cos^j(\theta)$ gives the following set of simultaneous equations,

$$(j=0) \quad \sum_{n=0}^{\infty} \left[\xi + (2n-1) \frac{\eta}{R} \right] a_{0,2n} R^{2n} = \tilde{\zeta} \Delta \mu \left(\frac{\pi R}{2l} - \frac{\pi^3 R^3}{12l^3} \right), \quad (\text{B.19})$$

$$(j=1) \quad \sum_{n=0}^{\infty} \left(\xi + 2n \frac{\eta}{R} \right) (a_{1,2n} - b_{0,2n+1}) R^{2n+1} = \tilde{\zeta} \Delta \mu \left(1 - \frac{\pi^2 R^2}{2l^2} \right), \quad (\text{B.20})$$

$$(j=2) \quad \sum_{k=0}^1 (-1)^k \sum_{n=k}^{\infty} \binom{n}{k} \left[\xi + (1+2n-2k) \frac{\eta}{R} \right] (a_{2-2k,2n} - b_{1-2k,2n+1}) R^{2(1+n-k)} = \tilde{\zeta} \Delta \mu \left(\frac{\pi^3 R^3}{4l^3} - \frac{\pi R}{l} \right), \quad (\text{B.21})$$

$$(j=3) \quad \sum_{k=0}^1 (-1)^k \sum_{n=k}^{\infty} \binom{n}{k} \left[\xi + (1+n-k) \frac{2\eta}{R} \right] (a_{3-2k,2n} - b_{2-2k,2n+1}) R^{3+2n-2k} = \tilde{\zeta} \Delta \mu \frac{\pi^2 R^2}{2l^2}, \quad (\text{B.22})$$

$$(j=4) \quad \sum_{k=0}^2 (-1)^k \sum_{n=k}^{\infty} \binom{n}{k} \left[\xi + (3+2n-2k) \frac{\eta}{R} \right] (a_{4-2k,2n} - b_{3-2k,2n+1}) R^{2(2+n-k)} = -\tilde{\zeta} \Delta \mu \frac{\pi^3 R^3}{6l^3} \quad (\text{B.23})$$

(all other values of j)

$$\sum_{k=0}^{\bar{j}} (-1)^k \sum_{n=k}^{\infty} \binom{n}{k} \left[\xi + (j+2n-2k-1) \frac{\eta}{R} \right] (a_{j-2k,2n} - b_{j-2k-1,2n+1}) R^{j+2n-2k} = 0. \quad (\text{B.24})$$

We use mathematical software to simultaneously solve eqs. (B.7), (B.8), (B.9), (B.11), (B.12), (B.5), (B.17), (B.19), (B.20), (B.21), (B.22), (B.23) and (B.24) for the finite case where we truncate the general solutions eqs. (15), (16) and (17) by assuming that $a_{m,n} = b_{m,n} = c_{m,n} = 0$ when $m+n \geq i$ where i is a finite integer. By solving at various values of i we find that the general solutions are attained for $i \geq 6$ because when coefficients that have $m+n > 6$ are included these are found to be 0. This truncation occurs because we have approximated the equations of motion to second order in r/l . More accurate solutions can be obtained by approximating these to higher order, and for each extra order included, the minimum value of i required for complete solutions increases by 1. However, to our knowledge, the solutions cannot be generalised analytically to solve for the infinite order case.

Finally, the complete analytical solutions are given by eqs. (B.25), (B.26), and (B.27).

$$\begin{aligned}
v_x = \zeta \Delta \mu \left\{ & -\frac{\pi R^2 \left[1 + \frac{\pi^2 R^2}{48 \eta l^2} (\xi R - 2\eta) \right]}{8l (\xi R + 2\eta)} - \frac{\left(1 - \frac{\pi^2 R^2}{4l^2} \right)}{2 (\xi R + 4\eta)} x + \frac{\pi \left[\xi R + 3\eta + \frac{\pi^2 R^2}{32 l^2} \left(\frac{(\xi R)^2}{3\eta} - \xi R - 6\eta \right) \right]}{2l (\xi R + 6\eta) (\xi R + 2\eta)} x^2 \right. \\
& + \frac{\pi \left[3\eta + \frac{\pi^2 R^2}{32 l^2} \left(\frac{(\xi R)^2}{\eta} + 9\xi R + 6\eta \right) \right]}{2l (\xi R + 6\eta) (\xi R + 2\eta)} y^2 + \frac{\left[\xi R + 8\eta - \frac{\pi^2 R^2}{2l^2} (\xi R + 6\eta) \right]}{2R^2 (\xi R + 4\eta) (\xi R + 8\eta)} x^3 + \frac{3 \left[\xi R + 8\eta - \frac{\pi^2 R^2}{l^2} \eta \right]}{2R^2 (\xi R + 4\eta) (\xi R + 8\eta)} x y^2 \\
& - \frac{3\pi \left[\xi R + 10\eta + \frac{\pi^2 R^2}{12 l^2} \left(\frac{(\xi R)^2}{12\eta} - \xi R - 15\eta \right) \right]}{8R^2 l (\xi R + 6\eta) (\xi R + 10\eta)} x^4 + \frac{5\pi \left[\xi R + 10\eta + \frac{\pi^2 R^2}{12 l^2} \left(\frac{(\xi R)^2}{4\eta} + 5\xi R + 27\eta \right) \right]}{8R^2 l (\xi R + 6\eta) (\xi R + 10\eta)} y^4 \\
& - \frac{3\pi \left[\xi R + 10\eta + \frac{\pi^2 R^2}{12 l^2} \left(\frac{(\xi R)^2}{4\eta} + 5\xi R + 15\eta \right) \right]}{4R^2 l (\xi R + 6\eta) (\xi R + 10\eta)} x^2 y^2 + \frac{\pi^2}{8R^2 l^2 (\xi R + 8\eta)} (x^5 - 5x y^4) \\
& \left. - \frac{\pi^3}{192R^2 l^3 (\xi R + 10\eta)} (5x^6 - 15x^4 y^2 - 45x^2 y^4 + 7y^6) \right\} \tag{B.25}
\end{aligned}$$

$$\begin{aligned}
v_y = \tilde{\zeta} \Delta \mu \left\{ & \frac{\left(1 - \frac{\pi^2 R^2}{4l^2} \right)}{2 (\xi R + 4\eta)} y - \frac{\pi \left[\xi R + 3\eta + \frac{\pi^2 R^2}{32 l^2} \left(\frac{(\xi R)^2}{3\eta} - \xi R - 6\eta \right) \right]}{l (\xi R + 6\eta) (\xi R + 2\eta)} x y - \frac{3 \left[\xi R + 8\eta - \frac{\pi^2 R^2}{2l^2} (\xi R + 6\eta) \right]}{2R^2 (\xi R + 4\eta) (\xi R + 8\eta)} x^2 y \right. \\
& - \frac{\left[\xi R + 8\eta - \frac{\pi^2 R^2}{l^2} \eta \right]}{2R^2 (\xi R + 4\eta) (\xi R + 8\eta)} y^3 + \frac{3\pi \left[\xi R + 10\eta + \frac{\pi^2 R^2}{12 l^2} \left(\frac{(\xi R)^2}{12\eta} - \xi R - 15\eta \right) \right]}{2R^2 l (\xi R + 6\eta) (\xi R + 10\eta)} x^3 y \\
& + \frac{\pi \left[\xi R + 10\eta + \frac{\pi^2 R^2}{12 l^2} \left(\frac{(\xi R)^2}{4\eta} + 5\xi R + 15\eta \right) \right]}{2R^2 l (\xi R + 6\eta) (\xi R + 10\eta)} x y^3 - \frac{\pi^2}{8R^2 l^2 (\xi R + 8\eta)} (5x^4 y - y^5) \\
& \left. + \frac{\pi^3}{192R^2 l^3 (\xi R + 10\eta)} (30x^5 y - 20x^3 y^3 - 18x y^5) \right\} \tag{B.26}
\end{aligned}$$

$$\begin{aligned}
P = c_{0,0} + \tilde{\zeta} \Delta \mu \left\{ & -\frac{\pi \xi R \left(1 - \frac{\pi^2 R^2}{12 l^2} \right)}{2l (\xi R + 2\eta)} x + \frac{3\eta \left(1 - \frac{\pi^2 R^2}{4l^2} \right)}{R^2 (\xi R + 4\eta)} x^2 - \frac{3\eta \left(1 + \frac{\pi^2 R^2}{12 \eta l^2} (\xi R + \eta) \right)}{R^2 (\xi R + 4\eta)} y^2 \right. \\
& - \frac{2\pi \eta \left(1 + \frac{\pi^2 R^2}{96 l^2} (\xi R - 6\eta) \right)}{R^2 l (\xi R + 6\eta)} (x^3 - 3x y^2) + \frac{5\pi^2 \eta}{8R^2 l^2 (\xi R + 8\eta)} (x^4 - 6x^2 y^2 + y^4) \\
& \left. - \frac{\pi^3 \eta}{8R^2 l^3 (\xi R + 10\eta)} (x^5 - 10x^3 y^2 + 5x y^4) \right\}. \tag{B.27}
\end{aligned}$$

C Governing equations for Lattice Boltzmann Simulations of an Active Droplet

The Lattice-Boltzmann simulations, used to obtain figure 3, are adapted from [19]. This section summarises the governing equations in these simulations.

Firstly, the free energy functional, which governs the passive state of the system, in summation notation is as follows:

$$\begin{aligned}
F[\phi, p_i] = \int d^3 r \left\{ & \frac{a}{4\phi_{cr}^4} \phi^2 (\phi - \phi_0)^2 + \frac{k_\phi}{2} |\nabla \phi|^2 \right. \\
& \left. - \frac{\alpha}{2} (\phi - \phi_{cr}) p_i p_i + \frac{\alpha}{4} (p_i p_i)^2 + \frac{K}{2} (\partial_i p_j) (\partial_i p_j) \right\}. \tag{C.1}
\end{aligned}$$

In this model, ϕ is the activity concentration, and so $\phi = 0$ in the passive phase, $\phi > \phi_{cr}$ in the active phase. The first term in eq. (C.1), with coefficient a , gives free energy minima for ϕ at $\phi = 0$ and $\phi = \phi_0 > \phi_{cr}$. The coefficient k_ϕ contributes to the interfacial tension, and α characterises the isotropic to nematic transition (this term couples $|\mathbf{p}| = 0$ to the passive phase and $|\mathbf{p}| = 1$ to the active phase). The final term is the distortion free energy from eq. (1) where K is the elastic constant in the one constant approximation $K_1 = K_2 = K_3 = K$ and we assume no specific anchoring at the boundary.

The total activity in the system is conserved, so the time evolution of ϕ is calculated using a convective-diffusion equation at each time-step:

$$\frac{\partial \phi}{\partial t} + (v_i \partial_i) \phi = M \partial_i \partial_i \frac{\delta F}{\delta \phi}, \tag{C.2}$$

where M is related to the diffusion. Using the same notation as eq. (5), the polarisation dynamics are governed by the following hydrodynamic equation:

$$\frac{\partial p_i}{\partial t} + (v_k \partial_k) p_i + \omega_{ij} p_j + \nu u_{ij} p_j = \frac{1}{\Gamma} h_i. \quad (\text{C.3})$$

This is equivalent to the polarisation equation in [5] with the active term λ_1 set to zero. In eq. (C.3), $\omega_{\alpha\beta}$ are components of the vorticity tensor and Γ is the rotational viscosity.

Lattice-Boltzmann techniques are used to satisfy the incompressible Navier-Stokes equations (the time dependent version of eqs. (6) and (7)),

$$\partial_i v_i = 0 \quad (\text{C.4})$$

$$\rho \left(\frac{\partial}{\partial t} + v_k \partial_k \right) v_i = \partial_j (\sigma_{ji}^{total} - P \delta_{ij}) - \xi v_i, \quad (\text{C.5})$$

where ξ is again the friction coefficient. The tensor σ^{total} is the stress tensor of eq. (5) plus the stress at the interface given by,

$$\sigma_{ij}^{interface} = \left(f - \phi \frac{\delta F}{\delta \phi} \right) \delta_{ij} - \frac{\partial f}{\partial (\partial_j \phi)} \partial_i \phi, \quad (\text{C.6})$$

where f is the free energy density.

We initialise the simulation by assuming an aligned polarisation field $\mathbf{p} = \hat{\mathbf{x}}$ inside a circular droplet in the active phase. The initial radius of the droplet is set to approximately 1/5 of the total grid size so that the drop is isolated and the boundaries are periodic to allow the droplet to migrate freely.